



Recent European drought extremes beyond Common Era background variability

Ulf Büntgen^{1,2,3,4}  , Otmar Urban², Paul J. Krusic^{1,5}, Michal Rybníček^{2,6}, Tomáš Kolář^{2,6}, Tomáš Kyncl⁷, Alexander Ač², Eva Koňasová⁶, Josef Čáslavský^{1,2} , Jan Esper^{2,8}, Sebastian Wagner⁹, Matthias Saurer⁴, Willy Tegel¹⁰, Petr Dobrovlný^{2,3}, Paolo Cherubini^{4,11}, Frederick Reinig⁸ and Miroslav Trnka^{1,2,12} 

Europe's recent summer droughts have had devastating ecological and economic consequences, but the severity and cause of these extremes remain unclear. Here we present 27,080 annually resolved and absolutely dated measurements of tree-ring stable carbon and oxygen ($\delta^{13}\text{C}$ and $\delta^{18}\text{O}$) isotopes from 21 living and 126 relict oaks (*Quercus* spp.) used to reconstruct central European summer hydroclimate from 75 BCE to 2018 CE. We find that the combined inverse $\delta^{13}\text{C}$ and $\delta^{18}\text{O}$ values correlate with the June–August Palmer Drought Severity Index from 1901–2018 at 0.73 ($P < 0.001$). Pluvials around 200, 720 and 1100 CE, and droughts around 40, 590, 950 and 1510 CE and in the twenty-first century, are superimposed on a multi-millennial drying trend. Our reconstruction demonstrates that the sequence of recent European summer droughts since 2015 CE is unprecedented in the past 2,110 years. This hydroclimatic anomaly is probably caused by anthropogenic warming and associated changes in the position of the summer jet stream.

The severe summer heat waves and drought spells in 2003, 2015 and 2018 affected Europe's agricultural, viticultural and silvicultural sectors^{1–5}. Reduced harvests, together with increased pathogens, insect outbreaks and forest mortality, have impacted economies, ecosystems and carbon cycle dynamics at various spatiotemporal scales⁶. Record-low river runoff constrained shipping traffic and even the cooling of nuclear power stations⁷. Climate-induced death tolls were highest in southern Europe⁸, where an estimated 70,000 people died in response to the unusually hot summer of 2003⁹. A further increase in the frequency and severity of heat waves under projected global warming implies a multitude of harmful direct and indirect impacts on human health^{10,11}.

Reconstructed and simulated European hydroclimate

Placing the wide range of ecological and societal consequences of Europe's most recent hydroclimatic extremes in the long-term context of pre-industrial variability depends on the dating precision and resolution, as well as the signal-to-noise ratio and overall timespan of the available proxy data. The Old World Drought Atlas (OWDA)¹², arguably the state-of-the-art tree-ring-based spatial field reconstruction of summer wetness and dryness over Europe and the Mediterranean Basin, is restricted to interannual and decadal variations between medieval times and 1978 CE (that is, the most recent four decades are not covered). And, during the first half of the Common Era, the OWDA does not capture the full range of natural hydroclimate variability. In addition to the various constraints of existing moisture-sensitive proxy records¹³, the current suite of palaeoclimatic Earth system model simulations is

limited in their ability to realistically estimate past precipitation and soil moisture fluctuations^{14,15}. Sensitivity studies with climate model simulations that use different combinations of external and internal forcing factors struggle to distinguish the dominant processes of synoptic summer droughts^{16,17}. This caveat is partly due to the coarse resolution of current Earth system models and the challenge of dynamically downscaling hydrological changes in the palaeoclimatic context. Although the importance of soil moisture and evapotranspiration for summer droughts has been acknowledged^{18,19}, and improvements have been made by forcing regional climate models with reanalysis data²⁰, Earth system models are still not able to mimic monthly soil moisture deficits at ecologically and economically relevant scales. In summary, the existing generation of proxy reconstructions and model simulations (or any combination thereof) are unable to place the alarming sequence of Europe's recent drought extremes in the context of Common Era hydroclimate variability, or quantify the relative roles of natural and anthropogenic forcing factors that conspire to amplify the severity of current and future extremes^{13,21}.

Hydroclimatic sensitivity of tree-ring stable isotopes

Here, we use 13,496 $\delta^{18}\text{O}$ measurements and 13,584 $\delta^{13}\text{C}$ measurements that are annually resolved and absolutely dated from 147 oaks (*Quercus* spp.) that grew over the past 2,110 years in what are today the Czech Republic and parts of south-eastern Bavaria (Fig. 1, Extended Data Fig. 1 and Supplementary Data 1). We argue that tree-ring stable isotopes (TRSI) are a superior archive for high-resolution reconstructions of hydroclimate variability in

¹Department of Geography, University of Cambridge, Cambridge, UK. ²Global Change Research Institute of the Czech Academy of Sciences (CzechGlobe), Brno, Czech Republic. ³Department of Geography, Faculty of Science, Masaryk University, Brno, Czech Republic. ⁴Swiss Federal Research Institute (WSL), Birmensdorf, Switzerland. ⁵Department of Physical Geography, Stockholm University, Stockholm, Sweden. ⁶Department of Wood Science and Technology, Faculty of Forestry and Wood Technology, Mendel University in Brno, Brno, Czech Republic. ⁷Moravian Dendro-Labor, Brno, Czech Republic. ⁸Department of Geography, Johannes Gutenberg University, Mainz, Germany. ⁹Helmholtz-Centre Geesthacht, Centre for Material and Coastal Research, Geesthacht, Germany. ¹⁰Chair of Forest Growth and Dendroecology, University of Freiburg, Freiburg, Germany. ¹¹Department of Forest and Conservation Sciences, Faculty of Forestry, University of British Columbia, Vancouver, British Columbia, Canada. ¹²Department of Agrosystems and Bioclimatology, Faculty of Agronomy, Mendel University in Brno, Brno, Czech Republic. [✉]e-mail: ulf.buentgen@geog.cam.ac.uk

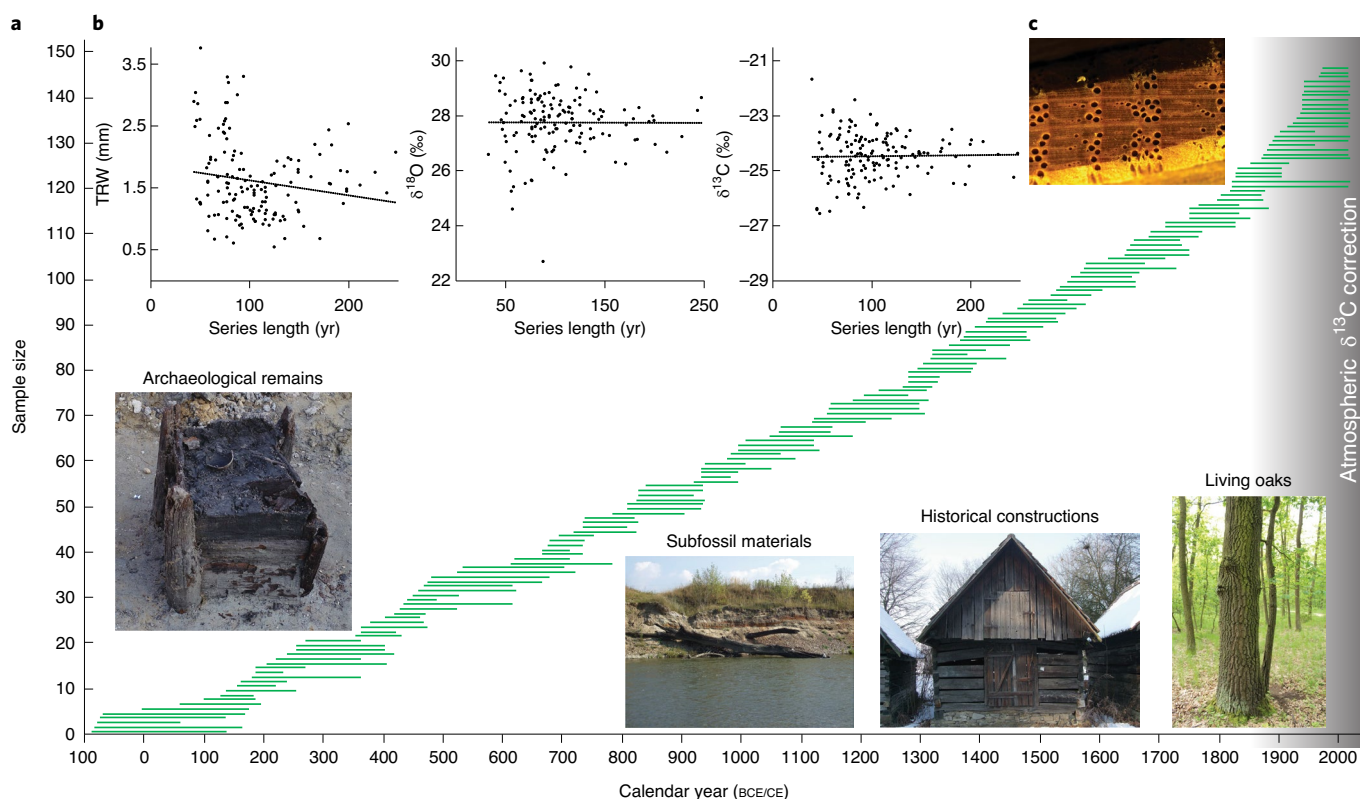


Fig. 1 | Growth characteristics and temporal coverage of the central European oak stable isotope dataset. **a**, Temporal distribution of 147 living, historical, archaeological and subfossil oaks (green bars). The photographs at the bottom show examples of archaeological remains, subfossil materials, historical constructions and living oaks, and the grey shading on the right refers to the industrial period during which anthropogenic fossil fuel emissions affect the isotopic composition of CO_2 . **b**, Annually resolved TRW (left), $\delta^{18}\text{O}$ (middle) and $\delta^{13}\text{C}$ (right) measurement series aligned by their cambial ages (series length). The mean TRW, $\delta^{18}\text{O}$ and $\delta^{13}\text{C}$ values are 1.6 mm, 27.8‰ and -24.4‰ , respectively (Extended Data Fig. 2). **c**, Microscopic amplification of an oak core sample that shows a sequence of well-defined tree rings. Non-pooled TRSI measurements were extracted exclusively from the latewood alpha cellulose (long-term behaviour is shown in Supplementary Fig. 1).

temperate areas where conventional tree-ring parameters often fail^{22,23}. Our new composite chronology integrates a total of 27,080 non-pooled TRSI measurements from latewood alpha cellulose. The wood material originates from 21 living oaks, which cover wide geographical and ecological ranges to avoid statistical overfitting during the calibration period²⁴. We also collected 126 core and disc samples from construction timbers, subfossil remains and archaeological excavations of the same genus. Sample replication between 75 BCE and 2018 CE, including year zero, ranges from 5–21 oaks (Fig. 1), with an average of 7.2 trees per year. The mean series length is 106 years with a standard deviation of 43 years (Extended Data Fig. 2). Sample selection resulted in enough overlap between the individual series and an equal distribution of juvenile and adult wood over time. The even sample distribution of living and relict oaks in space and time precludes any clustering and associated bias during both calibration and reconstruction²⁴. In contrast to the heteroscedastic oak tree-ring width (TRW) series (Fig. 1b), both carbon and oxygen TRSI measurements are free of age-related trends²², and therefore do not require standardization for chronology development (Methods). Calculated as the difference between annual $\delta^{13}\text{C}$ values in atmospheric CO_2 relative to a pre-industrial standard level of -6.4‰ , we applied a correction factor to the 31 most recent $\delta^{13}\text{C}$ series that extend beyond 1850 CE (ref.²⁵). This is necessary because the long-term change in the isotopic composition of CO_2 is not directly related to climate and would distort correlations to drought if unaccounted for. The correction for atmospheric $\delta^{13}\text{C}$ depletion from anthropogenic fossil fuel emissions

(that is, a change in the ratio between $^{13}\text{CO}_2$ and $^{12}\text{CO}_2$) was based on the compilation of ice core data until 1977 and direct measurements from Mauna Loa until 2014, and we used a linear regression to extrapolate annual $\delta^{13}\text{C}$ values afterwards. The raw TRSI measurement series reveal the expected degree of parameter-specific coherency between 91 BCE and 2018 CE (Supplementary Fig. 1). Variation between the individual $\delta^{13}\text{C}$ TRSI measurements is largest in the most recent decades and from around 200–600 CE. The individual $\delta^{18}\text{O}$ TRSI measurements exhibit increased variance around 200 CE and from 700–900 CE. Although the median and mean of the raw $\delta^{13}\text{C}$ and $\delta^{18}\text{O}$ values correlate at 0.92 and 0.93 with each other (Supplementary Fig. 1), the median is less affected by individual outliers.

Comparison of the inverse median of the individual $\delta^{18}\text{O}$ and $\delta^{13}\text{C}$ measurements, as well as the variance-stabilized average of all 294 TRSI values (147 oxygen and 147 carbon) against monthly and seasonal means of the self-calibrated Palmer Drought Severity Index (scPDSI)²⁶, reveals high correlations between the TRSI data and central European summer hydroclimate (Fig. 2). As the overall shape of the response patterns of the individual and combined TRSI values is almost identical (that is, no effects before and after the growing season), the combined $\delta^{13}\text{C}$ and $\delta^{18}\text{O}$ values (hereinafter compound TRSI) almost always exhibit a substantially higher drought signal. The inverse compound TRSI chronology correlates well (Pearson's $r > 0.7$) with monthly June, July and August scPDSI (1901–2018), as well as all seasonal combinations between March and October. The significant correlation of 0.73 ($P < 0.001$), found

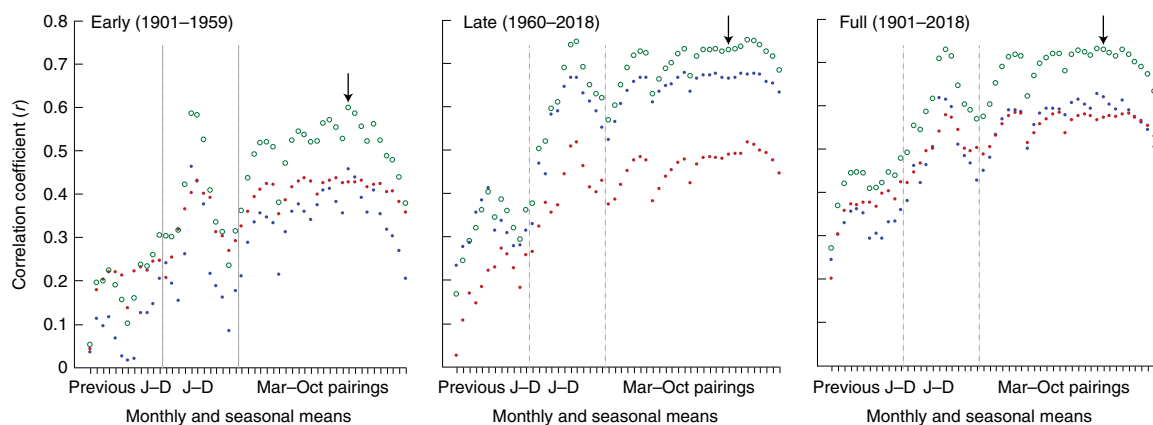


Fig. 2 | Temporal changes in the relation between oak stable isotopes and central European drought. Pearson's correlation coefficients (r) of the variance-stabilized inverse median of all 147 $\delta^{18}\text{O}$ and 147 $\delta^{13}\text{C}$ measurement series (blue and red dots) are shown, as well as their simple average (green circles), against monthly (from previous year January (J) to current year December (D)) and seasonal (all possible 28 monthly pairings between March and October of the growing season as described in the Extended Data Fig. 3) scPDSI averaged over central Europe (49–50° N and 15–18° E). Correlations are calculated over the early (left), late (middle) and full (right) periods of proxy–target overlap. Black arrows refer to the JJA mean.

between the compound TRSI and the mean June–August (JJA) scPDSI, changes to 0.58 and 0.75 when independently calculated over two contiguous instrumental periods: early (1901–1959) and late (1960–2018), respectively. The slightly lower correlations for carbon compared with oxygen in the late period could be caused by industrial pollution²⁷, whereas the recent increasing sensitivity of $\delta^{18}\text{O}$ could result from overall warmer and drier climate conditions. We assume that the lower-frequency hydroclimate signal in the oak TRSI is largely driven by temperature changes (Extended Data Fig. 3), and to a lesser extent by cloud cover and precipitation (Supplementary Fig. 2). Increasing temperatures and decreasing scPDSI since 1901 reveal similar first-order autocorrelation ($AC1=0.5$), whereas instrumental precipitation fluctuations basically resemble a ‘white noise’ process without temporal memory ($AC1=-0.1$)²⁸. It should be noted that the quantity and quality of instrumental precipitation measurements declines disproportionately back in time.

European summer drought from tree-ring stable isotopes

The original TRSI timeseries correlate with each other at 0.31 between 75 BCE and 2018 CE (Extended Data Fig. 4a). This positive association remains stable after 10 yr high- and low-pass filtering ($r=0.32$ and 0.30 , respectively), and the correlation further increases after 50 yr low-pass filtering ($r=0.37$). Both TRSI timeseries exhibit comparable first-order autocorrelation coefficients ($AC1=0.51$ and 0.73 for the oxygen and carbon values). Owing to a substantial degree of covariance between $\delta^{13}\text{C}$ and $\delta^{18}\text{O}$ (refs. ^{29,30}), as well as the enhanced hydroclimatic signal of our compound TRSI record and its notable interannual to multi-centennial coherency during the past 2,110 years (Extended Data Fig. 4a), we use the inverse average of the non-pooled, variance-stabilized $\delta^{13}\text{C}$ and $\delta^{18}\text{O}$ medians to reconstruct JJA scPDSI (Supplementary Data 2). Our evidence-based decision to combine both TRSI timeseries to reconstruct summer hydroclimate is corroborated by independent findings from both controlled plant experiments and theoretical fractionation models³¹, which suggest that moisture-limited conditions result in an enrichment of the heavy isotopes for both TRSI. Plants need to reduce stomatal conductance under drought to save water (which leads to higher $\delta^{13}\text{C}$), and although different fractionation mechanisms are involved, climate has a similar effect on $\delta^{18}\text{O}$. The influence of temperature on the oxygen isotopic signal of precipitation and higher leaf water isotope enrichment under increased vapour pressure deficit and thus drought are reflected in

$\delta^{18}\text{O}$ (ref. ³²). Consequently, the compound TRSI, which probably reflects different tree physiological processes³³, results in a stronger hydroclimatic signal compared with the two TRSI considered independently^{29,30}. Despite some degree of spatiotemporal and species-specific variation in the climate sensitivity of TRSI (ref. ³⁴), $\delta^{13}\text{C}$ and $\delta^{18}\text{O}$ values in temperate oaks generally reflect changes in growing season temperature and precipitation^{22,35,36}. The compound TRSI therefore provides a superior drought proxy that reflects the plant-relevant relationship with temperature and precipitation (that is, scPDSI)²⁶, which is corroborated by our findings.

Using a split period calibration/verification technique (Methods), our reconstruction captures the full range of instrumental summer hydroclimate between 1901 and 2018 (Fig. 3). All calibration/verification statistics confirm the temporal stability of the highly significant agreement between the reconstructed and measured JJA scPDSI (Extended Data Fig. 5). Most striking are the positive reduction of error/coefficient of efficiency and Durbin–Watson values of 0.52/0.24 and 2.31 of the final, full-period calibration model (Methods). An overall decrease in the quality and quantity of meteorological measurements back in time, however, may affect the slightly lower proxy–target fit in the first half of the twentieth century (Supplementary Fig. 2). Similar first-order autocorrelation ($AC1=0.5$) of both the proxy and target data further demonstrates the reconstruction skill on interannual to multi-decadal timescales. Although there is a slight proxy–target offset from 1914–1918, during the First World War, most of the measured extremes and longer-term trends are mirrored by the reconstruction (Fig. 3a). Wet and cold summers such as 1941 and 1997 coincide with increased cloud cover, precipitation and soil moisture (Supplementary Fig. 2), whereas the dry and warm summers of 1904, 1934 and 1976 are consistent with a decline in cloud cover, precipitation and soil moisture. Both the reconstructed and measured JJA scPDSI exhibit generally wetter conditions during the first half of the twentieth century, followed by a gradual drying trend since the early 1940s. Moreover, we find a clear negative relationship between measured and reconstructed JJA scPDSI and changes in annual crop yields during the twentieth century (Methods). Dry and warm conditions—not only wet and cold—can also affect the harvest of barley, wheat and grapes when exceeding plant physiological thresholds³⁷. Our reconstruction also seemingly contains a broad spatial component reflective of the average synoptic summer conditions over the Czech Republic and neighbouring regions in Poland, Germany, Austria, Hungary and Slovakia. (Fig. 3b). Spatial correlation maps of the proxy and

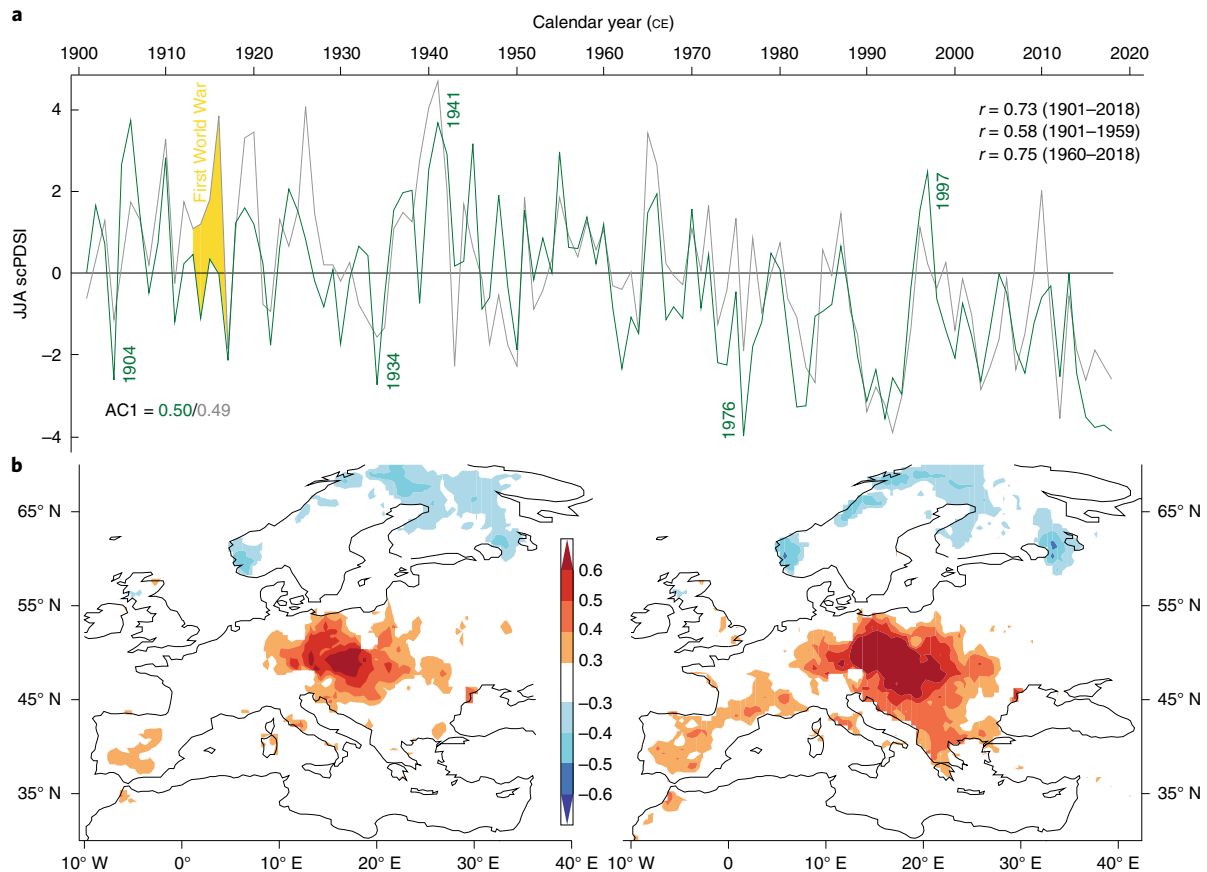


Fig. 3 | Temporal and spatial agreement between the oak stable isotopes and European summer drought. **a**, Actual (grey; averaged over 49–50° N and 15–18° E) and reconstructed (green; compound TRSI) JJA scPDSI. AC1 of the proxy and target data is provided at bottom left, whereas r values between the proxy and target data over the full and two early/late split periods are provided at the top right. **b**, High-resolution, 0.5° spatial correlation coefficients (colour scale) between the TRSI proxy data and the gridded European-wide scPDSI target data (left) and the regional average of the gridded scPDSI target data and European-wide gridded scPDSI target data (right) over the common period 1901–2018 CE.

target data jointly indicate a dipole structure between central Europe and northern Scandinavia. Continuous moisture supply during the growing season, when tree physiological processes are mainly controlled by atmospheric vapour pressure, probably contributes to the excellent signal-to-noise ratio of our new JJA scPDSI reconstruction.

We provide statistically robust evidence that the most recent drought extremes between 2015 and 2018 are not only unprecedented during the period of proxy–target overlap, but also in the context of the past 2,110 years (Fig. 4 and Supplementary Data 2). Clusters of exceptionally wet summers during Roman and medieval times, around 200, 720 and 1100 CE, are contrasted with prolonged dry spells centred over 40, 590 and 950 CE. The most striking drought episodes of the Common Era occurred from around 1490–1540 CE and from the mid-1970s to present (Fig. 4), with the corresponding extremes in 1508–1509 and from 2015–2018 CE, respectively (Extended Data Fig. 6). The five lowest reconstructed JJA scPDSI values are -4.81 , -4.76 , -4.67 , -4.53 and -4.52 in 1509, 1508, 2018, 2016 and 2017 CE, respectively. The driest 4-yr and 5-yr periods start in 2015 and 2014 CE, respectively. Moderately low soil moisture availability in the last century before the Common Era and the first century of the Common Era coincide with the end of the Celtic dominance in central Europe (that is, the Celtic Drought). Another period of prolonged aridity surrounds the Late Antique Little Ice Age in the sixth century³⁸ (that is, the LALIA Drought), when human migrations within and beyond Europe

peaked. Summers during the Great Moravian Empire, which ruled most of our study area from 833 to approximately 907 CE, were generally wetter (that is, the Early Medieval Pluvial). In contrast, the most pronounced drought spell in the early sixteenth century partly overlaps with the development of more than 70,000 artificial water bodies, fish farms and long-distance water channel systems across the Czech Lands (that is, the Renaissance Drought). Overall wetter conditions characterized the Little Ice Age from around 1600 CE to the late eighteenth century (the Little Ice Age Pluvial). On an annual scale, cold and wet summers match the sudden withdrawal of the Mongols from Hungary in 1242 CE (ref.³⁹), as well as the rapid spread of the Black Death between 1348 and 1351 CE (ref.⁴⁰), whereas warm and dry conditions are reconstructed for the so-called megadrought in 1540 CE. All these distinguishable high- to low-frequency signals are accompanied by asymmetric and temporally varying confidence limits (Fig. 4). The reconstruction error includes the annual standard error of all 27,080 non-pooled TRSI measurements between 75 BCE and 2018 CE, as well as the root mean squared error of the 1901–2018 calibration period (Methods). The reconstruction error is particularly narrow in the twentieth and early twenty-first century when sample size is highest (Extended Data Fig. 7a–c). The confidence limits are largest in the second century and again from around 610–820 CE, when the internal signal strength of $\delta^{13}\text{C}$ and $\delta^{18}\text{O}$ is lowest (Supplementary Fig. 1).

Our JJA scPDSI reconstruction is in line with existing precipitation-related proxies from Europe (Table 1 and

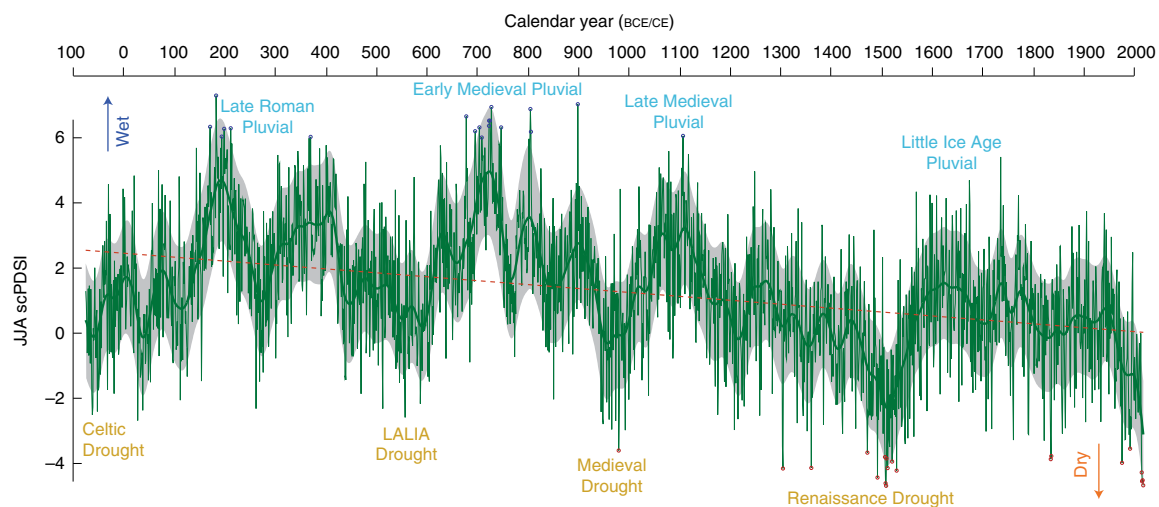


Fig. 4 | Reconstructed central European summer variability over the past 2,110 years. Reconstructed JJA scPDSI from 75 BCE to 2018 CE (Supplementary Data 2). The thick green curve is a 50 yr cubic smoothing spline of the annual values, and the red and blue circles show the 20 lowest and highest reconstructed values, respectively (Extended Data Fig. 6). The grey shading refers to the confidence limits after smoothing, and the dashed line represents the highly significant long-term drying trend ($y = -0.0012x + 2.4561$, $R^2 = 0.1281$).

Table 1 | Comparison of our new JJA scPDSI reconstruction with warm-season precipitation-related records and temperature palaeoclimatic records from central Europe

	This study	Brazdil et al. ⁴¹	Mozny et al. ⁴²	Cook et al. ¹²	Büntgen et al. ⁴³	Dobrovolny et al. ⁴⁴	Büntgen et al. ⁴⁵	Büntgen et al. ⁴³	Luterbacher et al. ⁴⁶
Proxy	TRSI	Documentary evidence	Grape harvest	TRW	TRW	Documentary evidence	MXD	TRW	TRW and MXD
Region	Central Europe	Czech Republic	Czech Republic	Czech Republic	Central Europe	Czech Republic	European Alps	Central Europe	Europe
Parameter	scPDSI	Z index	SPEI	scPDSI	precip.	temp.	temp.	temp.	temp.
Season	JJA	JJA	AMJJA	JJA	AMJ	JJA	JJAS	JJA	JJA
Period	75 BCE–2018 CE	1501–2014 CE	1499–2012 CE	1–2012 CE	398 BCE–2008 CE	1500–2016 CE	755–2004 CE	499 BCE–2003 CE	137 BCE–2003 CE
Original AC1	0.43	0.10	0.18	0.36	0.42	0.21	0.67	0.70	0.47
Original <i>r</i>		0.46	0.37	0.34	0.20	−0.39	−0.25	−0.23	−0.30
50 yr spline <i>r</i>		0.36	0.61	0.38	0.51	−0.48	−0.35	−0.32	−0.42

See Supplementary Figs. 3 and 4 for details. Pearson's *r* and AC1 were computed from 1500 CE to present. MXD, maximum latewood density; scPDSI, self-calibrated Palmer Drought Severity Index; Z index, short-term Palmer Index; SPEI, Standardized Precipitation-Evapotranspiration Index; original, unfiltered; precip., precipitation; temp., temperature.

Supplementary Fig. 3)^{12,41–43}. Positive correlations with four high-resolution hydroclimate reconstructions range from 0.20 to 0.46 for the original data (1500 CE–present), and increase to 0.38–0.61 after 50 yr smoothing. Negative correlations with four annually resolved temperature records^{43–46} range from −0.23 to −0.39, and increase to −0.32 to −0.48 after smoothing (Table 1 and Supplementary Fig. 4). In both cases, the highest agreement with our new reconstruction comes from documentary evidence of the Czech Lands^{41,44}. In contrast to the negative pre-industrial insolation signal found in a summer temperature reconstruction from northern Scandinavia⁴⁷, the physically driven long-term decline in our moisture record not only appears significant before 1850 CE (Extended Data Fig. 8), but also over the entire 2,110 years of the reconstruction. Similar long-term changes in soil moisture availability have been suggested by low-resolution stalagmite and pollen data from eastern China^{48–50}, but have so far been absent in the available 2,000-yr-long central European proxies^{12,46} (Extended Data Fig. 9).

Forcing factors of European summer droughts

The recent anthropogenic warming, antithetical to a long-term orbital summer cooling that is particularly strong at the high-northern latitudes⁴⁷, probably weakens the latitudinal temperature gradient and reduces mid-latitude moisture transport and net precipitation⁵¹. In contrast to findings from western Europe and the western Mediterranean Basin^{52,53}, we see no effect of large volcanic eruptions in the reconstructed JJA scPDSI (Extended Data Fig. 10). None of the four largest, best-documented and precisely dated historical eruptions—536 CE (unknown), 1257 CE (Samalas), 1783–1784 CE (Laki) and 1815 CE (Tambora)—seem to have affected central European summer hydroclimate at any detectable level (Extended Data Fig. 10a). A more systematic assessment of the 12 (17) largest volcanic eruptions⁵⁴ that occurred between 100 and 1200 CE (1200 and 1900 CE) also finds no substantial impact (Extended Data Fig. 10b). A decade-long drying trend is, however, found after 12 Icelandic eruptions. The absence of post-volcanic anomalies in our hydroclimate reconstruction is not surprising in the light of generally less

pronounced and spatially more variable precipitation responses to volcanic eruptions, and the inability of TRSI to capture severe ephemeral summer cooling. Anthropogenic greenhouse gas emissions and associated changes in internal atmospheric dynamics, such as an increase in anticyclonic blocking^{1–3}, most probably contributed to the recent cluster of central European heat waves and summer droughts between 2003 and 2018. Disentangling their relative roles, however, remains challenging. Both the location of the summer jet stream and the corresponding position and duration of high-pressure cells over northern and central Europe may affect the spatiotemporal scale of pan-European summer droughts⁵⁵. The relative contributions of atmospheric and ocean circulation patterns over the North Atlantic on European summer droughts, especially their preceding dynamical constraints during winter and spring, are still broadly unknown. Despite the general lack of negative forcing from solar minima and volcanic eruptions, possible drivers of the Renaissance Drought in the first decade of the sixteenth century also remain unclear. The coupled palaeoclimatic model simulations⁵⁶ from the Coupled Model Intercomparison Project Phase 5 and Palaeoclimate Modelling Intercomparison Project Phase 3 produce large differences in the regional extent and amplitude of soil moisture during the pre- and post-1850 periods (Supplementary Fig. 5). The current generation of Earth system models is not able to reproduce any long-term, pre-industrial moisture decline, and the simulated amplitude changes since 1850 differ substantially. Although much work remains before we can expect models to simulate regional hydroclimate variability more accurately, our study demonstrates the ability of TRSI to capture regional drought extremes and place them in a long-term context.

Online content

Any methods, additional references, Nature Research reporting summaries, source data, extended data, supplementary information, acknowledgements, peer review information; details of author contributions and competing interests; and statements of data and code availability are available at <https://doi.org/10.1038/s41561-021-00698-0>.

Received: 10 April 2020; Accepted: 19 January 2021;

Published online: 15 March 2021

References

- Schär, C. et al. The role of increasing temperature variability in European summer heatwaves. *Science* **427**, 332–336 (2004).
- Ionita, M. et al. The European 2015 drought from a climatological perspective. *Hydrol. Earth Syst. Sci.* **21**, 1397–1419 (2017).
- Kornhuber, K. et al. Extreme weather events in early summer 2018 connected by a recurrent hemispheric wave-7 pattern. *Environ. Res. Lett.* **14**, 054002 (2019).
- Fink, A. H. et al. The 2003 European summer heatwaves and drought – synoptic diagnosis and impacts. *Weather* **59**, 209–216 (2004).
- Laaha, G. et al. The European 2015 drought from a hydrological perspective. *Hydrol. Earth Syst. Sci.* **21**, 3001–3024 (2017).
- Ciais, P. et al. Europe-wide reduction in primary productivity caused by the heat and drought in 2003. *Nature* **437**, 529–533 (2005).
- Van Lanen, H. A. J. et al. Hydrology needed to manage droughts: the 2015 European case. *Hydrol. Process.* **30**, 3097–3104 (2016).
- Robine, J. M. et al. Death toll exceeded 70,000 in Europe during the summer of 2003. *C. R. Biol.* **331**, 171–178 (2008).
- García-Herrera, R., Díaz, J., Trigo, R. M., Luterbacher, J. & Fischer, E. M. A review of the European summer heat wave of 2003. *Crit. Rev. Environ. Sci. Technol.* **40**, 267–306 (2010).
- Haines, A., Koats, R. S., Campbell-Lendrum, D. & Corvalan, C. Climate change and human health: impacts, vulnerability, and mitigation. *Lancet* **367**, 2101–2109 (2006).
- Amengual, A. et al. Projections of heat waves with high impact on human health in Europe. *Glob. Planet. Change* **119**, 71–84 (2014).
- Cook, E. R. et al. Old World megadroughts and pluvials during the Common Era. *Sci. Adv.* **1**, e150056 (2015).
- Ljungqvist, F. C. et al. Northern Hemisphere hydroclimate variability over the past twelve centuries. *Nature* **532**, 94–98 (2016).
- Gomez-Navarro, J. J., Montavez, J. P., Wagner, S. & Zorita, E. A regional climate palaeosimulation for Europe in the period 1500–1990. Part 1: model validation. *Clim. Past* **9**, 1667–1682 (2013).
- Gomez-Navarro, J. J. et al. A regional climate palaeosimulation for Europe in the period 1500–1990. Part 2: shortcomings and strengths of models and reconstructions. *Clim. Past* **11**, 1077–1095 (2015).
- Frankcombe, L. M., England, M. H., Mann, M. E. & Steinman, B. A. Separating internal variability from the externally forced climate response. *J. Clim.* **28**, 8184–8202 (2015).
- Ryu, J. H. & Hayhoe, K. Observed and CMIP5 modeled influence of large-scale circulation on summer precipitation and drought in the South-Central United States. *Clim. Dynam.* **49**, 4293–4310 (2017).
- Fischer, E. M. & Schär, C. Future changes in daily summer temperature variability: driving processes and role for temperature extremes. *Clim. Dynam.* **33**, 917–935 (2009).
- Seneviratne, S. I. et al. Investigating soil moisture–climate interactions in a changing climate: a review. *Earth-Sci. Rev.* **99**, 125–161 (2010).
- Barella-Ortiz, A. & Quintana-Seguí, P. Evaluation of drought representation and propagation in regional climate model simulations across Spain. *Hydrol. Earth Syst. Sci.* **23**, 5111–5131 (2019).
- Ljungqvist, F. C. et al. Warm-season temperature and hydroclimate co-variability across Europe since 850 CE. *Environ. Res. Lett.* **14**, 084015 (2019).
- Büntgen, U. et al. No age trends in oak stable isotopes. *Paleocean. Paleoclim.* **34**, e2019PA003831 (2020).
- Urban, O. et al. The dendroclimatic value of oak stable isotopes. *Dendrochronologia* **65**, 125804 (2021).
- Tegel, W., Vanmoerkerke, J. & Büntgen, U. Updating historical tree-ring records for climate reconstruction. *Quat. Sci. Rev.* **29**, 1957–1959 (2010).
- Belmecheri, S. & Lavergne, A. Compiled records of atmospheric CO₂ concentrations and stable carbon isotopes to reconstruct climate and derive plant ecophysiological indices from tree rings. *Dendrochronologia* **63**, 125748 (2020).
- van der Schrier, G., Briffa, K. R., Jones, P. D. & Osborn, T. J. Summer moisture availability across Europe. *J. Clim.* **19**, 2819–2834 (2006).
- Boettger, T., Haupt, M., Friedrich, M. & Waterhouse, J. S. Reduced climate sensitivity of carbon, oxygen and hydrogen stable isotope ratios in tree-ring cellulose of silver fir (*Abies alba* Mill.) influenced by background SO₂ in Franconia (Germany, Central Europe). *Environ. Pollut.* **185**, 281–294 (2014).
- Bunde, A., Büntgen, U., Ludescher, J., Luterbacher, J. & von Storch, H. Is there memory in precipitation? *Nat. Clim. Change* **3**, 174–175 (2013).
- Saurer, M., Aellen, K. & Siegwolf, R. Correlating δ¹³C and δ¹⁸O in cellulose of trees. *Plant Cell Environ.* **20**, 1543–1550 (1997).
- Masson-Delmotte, V. et al. Changes in European precipitation seasonality and in drought frequencies revealed by a four-century-long tree-ring isotopic record from Brittany, western France. *Clim. Dynam.* **24**, 57–69 (2005).
- Farquhar, G. D., Ehleringer, J. R. & Hubick, K. T. Carbon isotope discrimination and photosynthesis. *Annu. Rev. Plant Physiol. Plant Mol. Biol.* **40**, 503–537 (1989).
- Roden, J. S., Lin, G. & Ehleringer, J. R. A mechanistic model for interpretation of hydrogen and oxygen isotope ratios in tree-ring cellulose. *Geochim. Cosmochim. Acta* **64**, 21–35 (2000).
- Scheidegger, Y., Saurer, M., Bahn, M. & Siegwolf, R. Linking stable oxygen and carbon isotopes with stomatal conductance and photosynthetic capacity: a conceptual model. *Oecologia* **125**, 350–357 (2000).
- Treydte, K. et al. Signal strength and climate calibration of a European tree-ring isotope network. *Geophys. Res. Lett.* **34**, L24302 (2007).
- Young, G. H. F. et al. Oxygen stable isotope ratios from British oak tree-rings provide a strong and consistent record of past changes in summer rainfall. *Clim. Dynam.* **45**, 3609–3622 (2015).
- Labuhn, I. et al. French summer droughts since 1326 CE: a reconstruction based on tree ring cellulose δ¹⁸O. *Clim. Past* **12**, 1101–1117 (2016).
- Trnka, M. et al. Mitigation efforts will not fully alleviate the increase in water scarcity occurrence probability in wheat-producing areas. *Sci. Adv.* **5**, eaau2406 (2019).
- Büntgen, U. et al. Cooling and societal change during the Late Antique Little Ice Age from 536 to around 660 AD. *Nat. Geosci.* **9**, 231–236 (2016).
- Büntgen, U. & Di Cosmo, N. Climatic and environmental aspects of the Mongol withdrawal from Hungary in 1242 CE. *Sci. Rep.* **6**, 25606 (2016).
- Schmid, B. V. et al. Climate-driven introduction of the Black Death and successive plague reintroductions into Europe. *Proc. Natl Acad. Sci. USA* **112**, 3020–3025 (2015).
- Brázdil, R. et al. Documentary and instrumental-based drought indices for the Czech Lands back to AD 1501. *Clim. Res.* **70**, 103–117 (2016).
- Mozny, M. et al. Drought reconstruction based on grape harvest dates for the Czech Lands. 1499–2012. *Clim. Res.* **70**, 119–132 (2016).
- Büntgen, U. et al. 2500 years of European climate variability and human susceptibility. *Science* **331**, 578–582 (2011).

44. Dobrovolny, P. et al. Monthly, seasonal and annual temperature reconstructions for Central Europe derived from documentary evidence and instrumental records since AD 1500. *Clim. Change* **101**, 69–107 (2010).
45. Büntgen, U., Frank, D. C., Nievergelt, D. & Esper, J. Summer temperature variations in the European Alps, AD 755–2004. *J. Clim.* **19**, 5606–5623 (2006).
46. Luterbacher, J. et al. European summer temperatures since Roman times. *Environ. Res. Lett.* **11**, 024001 (2016).
47. Esper, J. et al. Orbital forcing of tree-ring data. *Nat. Clim. Change* **2**, 862–866 (2012).
48. Wang, Y. et al. The Holocene Asian monsoon: links to solar changes and North Atlantic climate. *Science* **308**, 854–857 (2005).
49. Chen, F. et al. East Asian summer monsoon precipitation variability since the last deglaciation. *Sci. Rep.* **5**, 11186 (2015).
50. Cheng, H. et al. The Asian monsoon over the past 640,000 years and ice age terminations. *Nature* **534**, 640–646 (2016).
51. Routson, C. C. et al. Mid-latitude net precipitation decreased with Arctic warming during the Holocene. *Nature* **568**, 83–87 (2019).
52. Büntgen, U. et al. New tree-ring evidence from the Pyrenees reveals western Mediterranean climate variability since medieval times. *J. Clim.* **30**, 5295–5318 (2017).
53. Rao, M. P. et al. European and Mediterranean hydroclimate responses to tropical volcanic forcing over the last millennium. *Geophys. Res. Lett.* **44**, 5104–5112 (2017).
54. Toohey, M. & Sigl, M. Volcanic stratospheric sulfur injections and aerosol optical depth from 500 BCE to 1900 CE. *Earth Syst. Sci. Data* **9**, 809–831 (2017).
55. García-Herrera, R. et al. The European 2016/2017 drought. *J. Clim.* **32**, 3169–3187 (2019).
56. Braconnot, P. et al. Evaluation of climate models using palaeoclimatic data. *Nat. Clim. Change* **2**, 417–424 (2012).

Publisher's note Springer Nature remains neutral with regard to jurisdictional claims in published maps and institutional affiliations.

© The Author(s), under exclusive licence to Springer Nature Limited 2021

Methods

Dendrochronological data. Following a random sampling design to avoid statistical overfitting during the calibration period²⁴, the material used in this study represents the natural oak distribution in the Czech Republic and south-eastern Bavaria (Extended Data Fig. 1). The samples are composed of two main oak genera, *Q. robur* and *Q. petraea*, which are the most widespread oak genera across central Europe. The Bohemian and Moravian lowlands in the western and eastern parts of the Czech Republic are characterized by relatively warm and dry climate conditions. Both regions exhibit annual temperature means of $\sim 9\text{--}10^\circ\text{C}$ and annual precipitation totalling $\sim 450\text{--}500\text{ mm}$. Owing to substantial summer evapotranspiration²⁷, oak growth is mainly limited by soil moisture availability during the vegetation period from late spring to early autumn^{58–60}, with the main water shortage usually occurring between June and August.

A single increment core was extracted at $\sim 1.3\text{ m}$ stem height from each of 21 oaks at 7 different localities between 170 and 495 m above sea level (Extended Data Fig. 1). Across the Czech Republic and neighbouring south-eastern Bavaria, core and disc samples from 136 historical, subfossil and archaeological features were also collected. Much of the historical material originates from belfry constructions in church towers, whereas the archaeological samples were extracted in close collaboration with several commercial entities during rescue excavations. Subfossil oaks were excavated from gravel and sand pits along the Elbe, Morava, Oder and Vltava rivers (Extended Data Fig. 1). Ring widths of all 147 samples were measured using a VIAS TimeTable measuring system (SCIEM) at a precision of 0.01 mm. TRW measurements were synchronized and cross-dated visually using PAST4 (ref. 61) and the results were statistically controlled via COFECHA (ref. 62). The most recent version of the Czech oak TRW composite chronology^{59,63} was used as the reference chronology for cross-dating.

Isotopic data. The latewood alpha cellulose of each tree ring was carefully split with a scalpel under a stereomicroscope. For isotopic measurements^{25,29}, we followed the modified Jayme–Wise isolation method⁶⁴. Originating from either cores or discs, the $\sim 0.5\text{-mm}$ -wide individual wood samples were packed into Teflon filter bags and washed with a 5% NaOH solution twice for 2 h at 60°C , followed by an additional wash with 7% NaClO₂ solution for another 30 h at 60°C . Acetic acid (99.8%) was added to the solution to keep the pH between 4 and 5. After washing, the bags with extracted cellulose were rinsed three times in hot distilled water (90°C). Each sample was dried subsequently at 50°C for 24 h, locked in Eppendorf microtubes and stored in the dark under temperature-controlled conditions at 21°C before any further analysis.

For the independent determination of $\delta^{13}\text{C}$ and $\delta^{18}\text{O}$, alpha cellulose samples weighing between 0.2 and 1.0 mg were placed in tin and silver capsules, respectively. For $\delta^{13}\text{C}$ ($\delta^{18}\text{O}$), samples were combusted (pyrolysed) in CO₂ (CO) at 960°C ($1,450^\circ\text{C}$). Stable isotopes in the CO₂ and CO gases were measured in a continuous flow isotope ratio mass spectrometer ISOPRIME100 (Isoprime). Before each run of new isotopic measurements, the ion source of the mass spectrometer was centred, tuned and tested for stability (standard deviation $\leq 0.04\text{‰}$ on 10 pulses over 3 consecutive runs) and linearity ($\leq 0.03\text{‰ nA}^{-1}$) over the entire range of expected ion currents obtainable from the measurements of the test samples. The standard deviation was $\leq 0.06\text{‰}$ for $\delta^{13}\text{C}$ and $\leq 0.10\text{‰}$ for $\delta^{18}\text{O}$ on 5 consecutive measurements of the same alpha cellulose sample. The system was calibrated using certified reference materials with known isotopic ratios from the International Atomic Energy Agency (IAEA) and the United States Geological Survey (USGS). The $\delta^{13}\text{C}$ values were referenced to caffeine (IAEA-600) and graphite (USGS24). The $\delta^{18}\text{O}$ values were referenced to benzoic acid (IAEA-601 and IAEA-602). The $\delta^{13}\text{C}$ and $\delta^{18}\text{O}$ values (in ‰) were calculated as the deviation from the Vienna Pee Dee Belemnite (VPDB) and Vienna Standard Mean Ocean Water (VSMOW) standards, respectively, according to the formula $R = (R_{\text{sample}}/R_{\text{standard}} - 1) \times 1,000$, where R is the ratio of the heavy to light isotope ($^{13}\text{C}/^{12}\text{C}$, $^{18}\text{O}/^{16}\text{O}$). A correction factor for atmospheric $\delta^{13}\text{C}$ depletion from anthropogenic fossil fuel emissions was applied to the 31 $\delta^{13}\text{C}$ carbon series that have values after 1850 CE (ref. 25).

Climate reconstruction. As none of the TRSI values exhibit any statistically discernible long-term trend over their lifespan (Fig. 1b and Supplementary Fig. 1), which is in line with recent evidence^{22,23}, we calculated the median of the 147 $\delta^{13}\text{C}$ measurements and the median of the corresponding $\delta^{18}\text{O}$ measurements for each year between 75 BCE and 2018 CE (including year zero). After normalization (that is, all timeseries transformed to have a mean of zero and a standard deviation of one), the variance of the two median records was stabilized according to their 30 yr moving standard deviation (that is, the original values were divided by their standard deviations)⁶⁵. The inverse average of the non-pooled, variance-stabilized $\delta^{13}\text{C}$ and $\delta^{18}\text{O}$ median timeseries was used as final input data for the JJA scPDSI reconstruction from 75 BCE to 2018 CE (Extended Data Fig. 4c).

To test the robustness of our compound TRSI record, we produced a composite chronology of the combined 147 $\delta^{18}\text{O}$ and 147 $\delta^{13}\text{C}$ measurement series in one single run of the regional curve standardization (RCS) and signal-free (SF) detrending methodologies^{66–68}, as implemented in the SF chronology development program RCSsigFree_v45h (ref. 69). The initial RCS curve was derived using an age-dependent spline, with an initial frequency response of 40 yr (ref. 70) and applied within the SF framework to compute simple ratios from each sample's

radial time series of TRSI measurements. The variance of the final TRSI chronology was stabilized using the program's default running Rbar option with a window length of 51 yr and the optional age-dependent spline stabilization^{67,71}. Correlating at 0.98 with our original non-pooled, variance-stabilized compound TRSI chronology that uses the average of the non-standardized carbon and oxygen medians, the RCS-SF chronology confirmed the high- to low-frequency skill of our record.

On the basis of the initial non-pooled, variance-stabilized compound TRSI chronology, the final JJA scPDSI reconstruction was produced following the split period, a reconstruction methodology introduced by Cook et al.⁷² and expanded on in a later paper¹² without the principle component expansion module. The process began with a calibration and verification exercise using the original (raw) and prewhitened chronology (predictor) and drought (predictand) values over the period 1901–1959. This was the early period of the split period calibration and verification test. If both regression experiments, using the raw and prewhitened data, calibrated and verified significantly ($P < 0.05$ or less), the same experiment was repeated between the original predictand data and the prewhitened predictor data that had the persistence structure of the predictand given to it. If the early-period, persistence-enhanced predictor data also calibrated and verified significantly, then this rigorous three-part testing was repeated a second time with the withheld data over the late period (1960–2018) and a final time for the entire common period (1901–2018). For obvious reasons, there are no independent verification statistics available for the final reconstruction, consequently diagnostic indicators of model fit such as the calibration correlation and verification R^2 , as well as the verification period coefficient of efficiency and verification period reduction of error, will be the same or close to the same value. The little difference that may exist was due to the added persistence contributed by the predictand. The calibration and verification statistics for the equally long early and late periods (1901–1959 and 1960–2018) and the final full-period calibration (1901–2018) are presented in Extended Data Fig. 5.

Data availability statement

The raw tree-ring stable isotope measurements (Supplementary Data 1) and the final drought reconstruction (Supplementary Data 2) are freely available from the NOAA National Centers for Environmental Information (NCEI) at <https://www.ncdc.noaa.gov/paleo/study/32292>.

References

- Dobrovolný, P., Brázdil, R., Trnka, M., Kotyza, O. & Valášek, H. Precipitation reconstruction for the Czech Lands, AD 1501–2010. *Int. J. Climatol.* **35**, 1–14 (2015).
- Büntgen, U. et al. Tree-ring indicators of German summer drought over the last millennium. *Quat. Sci. Rev.* **29**, 1005–1016 (2010).
- Dobrovolný, P. et al. May–July precipitation reconstruction from oak tree-rings for Bohemia (Czech Republic) since AD 1040. *Int. J. Climatol.* **38**, 1910–1924 (2017).
- Rybníček, M. et al. Oak (*Quercus* spp.) response to climate differs more among sites than among species in central Czech Republic. *Dendrobiology* **75**, 55–65 (2016).
- Knibbe, B. *Personal Analysis System for Tree-ring Research 4—Instruction Manual* (SCIEM, 2004).
- Gissino-Mayer, H. D. Evaluating crossdating accuracy: a manual and tutorial for the computer program COFECHA. *Tree Ring Res.* **57**, 205–221 (2001).
- Prokop, O. et al. On the paleoclimatic potential of a millennium-long oak ring width chronology from Slovakia. *Dendrochronologia* **40**, 93–101 (2016).
- Boettger, T. et al. Wood cellulose preparation methods and mass spectrometric analyses of $\delta^{13}\text{C}$, $\delta^{18}\text{O}$, and nonexchangeable $\delta^2\text{H}$ values in cellulose, sugar, and starch: an interlaboratory comparison. *Anal. Chem.* **79**, 4603–4612 (2007).
- Frank, D., Esper, J. & Cook, E. R. Adjustment for proxy number and coherence in a large-scale temperature reconstruction. *Geophys. Res. Lett.* **34**, L16709 (2007).
- Briffa, K. R. et al. Fennoscandian summers from AD 500: temperature changes on short and long timescales. *Clim. Dynam.* **7**, 111–119 (1992).
- Esper, J., Cook, E. R., Krusic, P. J., Peters, K. & Schweingruber, F. H. Tests of the RCS method for preserving low-frequency variability in long tree-ring chronologies. *Tree Ring Res.* **59**, 81–98 (2003).
- Melvin, T. M. & Briffa, K. R. A “signal-free” approach to dendroclimatic standardisation. *Dendrochronologia* **26**, 71–86 (2008).
- Cook, E. R. & Krusic, P. J. RCSsigFree_v45h: a signal-free chronology development and analysis tool for dendrochronology (Lamont-Doherty Earth Observatory, 2007); <https://www.ldeo.columbia.edu/tree-ring-laboratory/resources/software>
- Melvin, T. M., Briffa, K. R., Nicolussi, K. & Grabner, M. Time-varying-response smoothing. *Dendrochronologia* **25**, 65–69 (2007).
- Osborn, T. J., Briffa, K. R. & Jones, P. D. Adjusting variance for sample size in tree-ring chronologies and other regional mean timeseries. *Dendrochronologia* **15**, 89–99 (1997).

72. Cook, E. R., Meko, D. M., Stahle, D. W. & Cleaveland, M. K. Drought reconstructions for the continental United States. *J. Clim.* **12**, 1145–1162 (1999).
73. Coplen, T. B. Discontinuance of SMOW and PDB. *Nature* **375**, 285 (1995).
74. Hamed, K. H. & Rao, A. R. A modified Mann-Kendall trend test for autocorrelated data. *J. Hydrol.* **204**, 182–196 (1998).

Acknowledgements

The work was supported by the Czech Republic Grant Agency (grant numbers 17-22102S and 18-11004S), and the SustES project—Adaptation strategies for sustainable ecosystem services and food security under adverse environmental conditions (CZ.02.1.01/0.0/0.0/16_019/0000797). U.B. and J.E. received funding from the ERC project Monostar (grant number AdG 882727) and W.T. acknowledges the German Research Foundation (grant number TE 613/3-2). Relict oak samples from Bavaria were collected and cross-dated by F. Herzig, and I. Roshka and N. Pernicová contributed to sample preparation.

Author contributions

U.B. and M.T. designed the study. U.B. and P.J.K. performed the analyses and wrote the manuscript. M.R., T. Kolář, T. Kyncl and E.K. developed the Czech oak tree-ring dataset and prepared samples for isotopic analyses. O.U., A.A. and J.Č. processed and measured

the stable isotopes. P.J.K. helped to develop the hydroclimatic reconstruction and S.W. provided model data and interpretation. J.E., M.S., W.T., P.D., P.C., F.R. and M.T. helped to place the results in a wider physiological, climatological and historical context. All authors provided critical discussion, helped to write and revise the manuscript and approved its submission.

Competing interests

The authors declare no competing interests.

Additional information

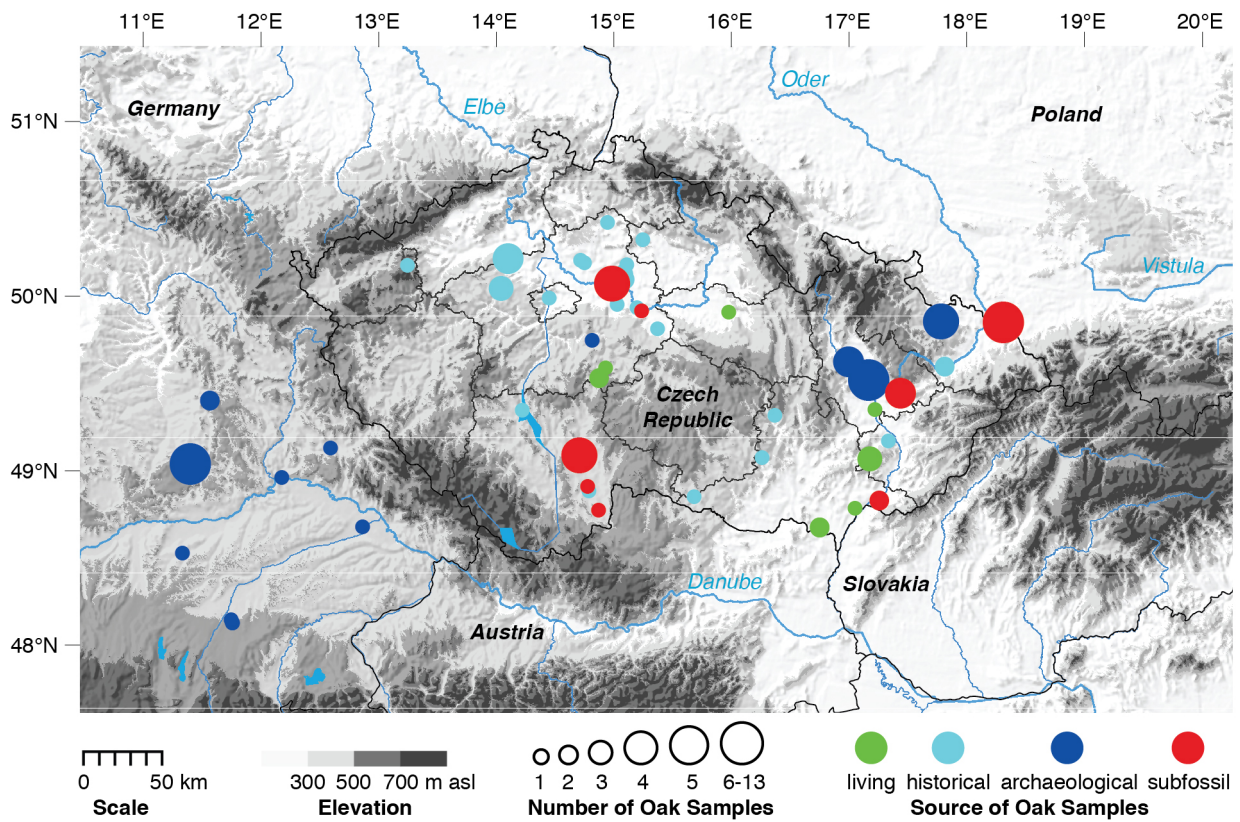
Extended data is available for this paper at <https://doi.org/10.1038/s41561-021-00698-0>.

Supplementary information The online version contains supplementary material available at <https://doi.org/10.1038/s41561-021-00698-0>.

Correspondence and requests for materials should be addressed to U.B.

Peer review information *Nature Geoscience* thanks Cody Routson and the other, anonymous, reviewer(s) for their contribution to the peer review of this work. Primary Handling Editor: James Super.

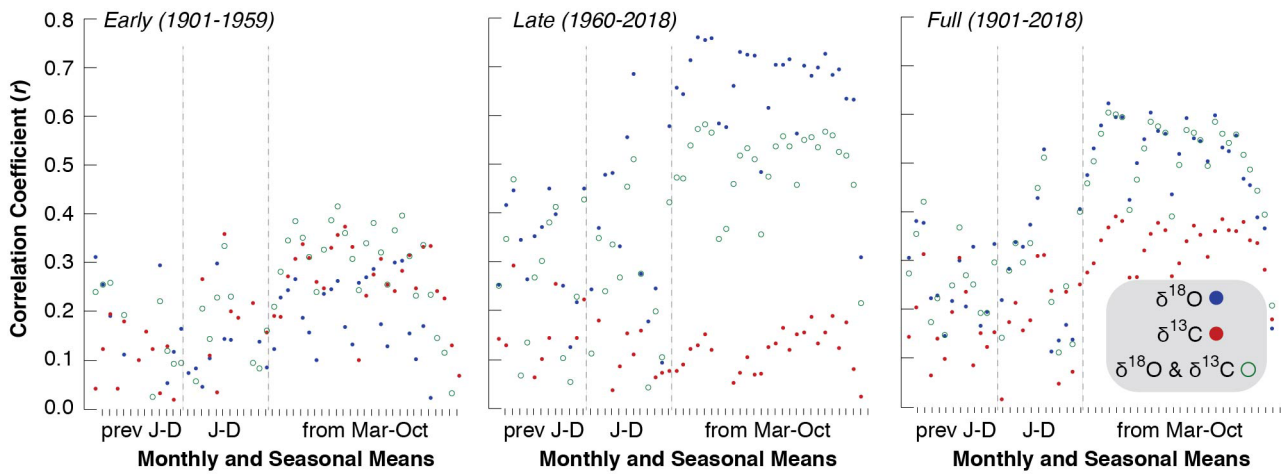
Reprints and permissions information is available at www.nature.com/reprints.



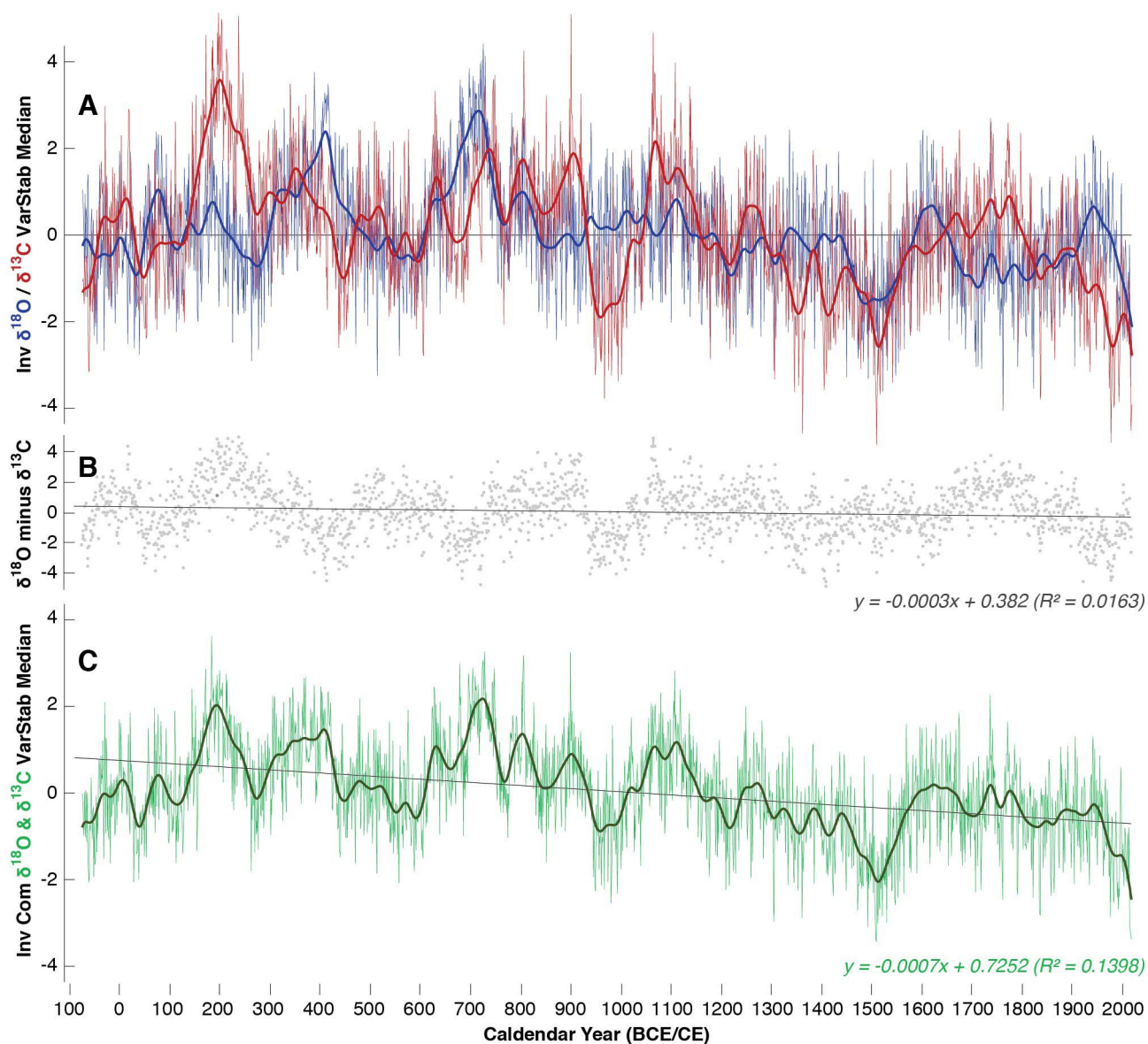
Extended Data Fig. 1 | Oak network. Spatial distribution of 147 living, historical, archaeological and subfossil oaks between 91 BCE and 2018 CE, for which TRW, $\delta^{18}\text{O}$ and $\delta^{13}\text{C}$ were measured at annual resolution. While the vast majority of samples originates from the Czech Republic, a few archaeological samples come from Bavaria in south-eastern Germany.

	series	years	start	end	msl	min	mean	max	stdev	sens	ac1
13C	147	2110	91 BCE	2018 CE	104	-26.572	-24.472	-21.695	0.795	0.021	0.572
13Ccorr	147	2110	91 BCE	2018 CE	104	-26.487	-24.302	-20.099	0.789	0.021	0.567
O18	147	2110	91 BCE	2018 CE	102	23.435	27.752	29.904	1.225	0.421	0.222
Compound TRSI	294	2110	91 BCE	2018 CE	103	-03.340	-00.047	03.594	1.222	0.220	0.652
TRW	147	2110	91 BCE	2018 CE	106	00.542	01.613	03.752	0.634	0.212	0.631

Extended Data Fig. 2 | Dendro inventory. Number of individual tree-ring samples (series), the total chronology length and its start and end year (year, start, end), the mean series length (msl), the minimum, mean and maximum raw measurement values (min, mean, max), as well as the standard deviation, mean sensitivity and first-order autocorrelation coefficient (stdev, sens, ac1), of the four dendro parameters: $\delta^{13}\text{C}$, $\delta^{13}\text{C}$ corrected, $\delta^{18}\text{O}$ and tree-ring width (13C, 13Ccorr, 18O, TRW). The compound TRSI data are z-scores (mean of zero and standard deviation of one). Carbon and oxygen isotope ratios are reported in per mil (‰) using the usual delta (δ) notation relative to the VPDB ($\delta^{13}\text{C}$) and VSMOW ($\delta^{18}\text{O}$) standards⁷³.



Extended Data Fig. 3 | Temperature sensitivity. Pearson's correlation coefficients between the non-standardized $\delta^{18}\text{O}$ (blue dots) and $\delta^{13}\text{C}$ (red dots) records (using the median of the individual measurements), as well as their simple average (green circles), and monthly (from previous year January to current year December) and seasonal (all possible 28 monthly pairings between March and October of the growing season: Mar-Apr, Mar-May, Mar-Jun, Mar-Jul, Mar-Aug, Mar-Sep, Mar-Oct, Apr-May, Apr-Jun, Apr-Jul, Apr-Aug, Apr-Sep, Apr-Oct, May-Jun, May-Jul, May-Aug, May-Sep, May-Oct, Jun-Jul, Jun-Aug, Jun-Sep, Jun-Oct, Jul-Aug, Jul-Sep, Jul-Oct, Aug-Sep, Aug-Oct, Sep-Oct) temperature averages over 49–50°N and 15–18°E. Correlations are calculated over the early, late and full period of proxy-target overlap (from left to right).



Extended Data Fig. 4 | Isotopic behaviour. (a) Comparison of the non-standardized, inverse $\delta^{18}\text{O}$ record (blue) against the non-standardized, inverse and corrected $\delta^{13}\text{C}$ records (red) using the median of the individual measurements. (b) Difference between the annual $\delta^{18}\text{O}$ and $\delta^{13}\text{C}$ values, with the straight line referring to their long-term trend (equation in brackets). (c) Simple average and long-term trend of the annual $\delta^{18}\text{O}$ and $\delta^{13}\text{C}$ data. All timeseries cover the period 75 BCE to 2018 CE, during which at least ten samples are included each year. The smoothed curves in (a) and (c) are 50-year low-pass filters.

	Pearson		Robust		Spearman		RE	CE	Xprod Mean	
Full Calibration										
	<i>Corr</i>	<i>Pct</i>	<i>Corr</i>	<i>Pct</i>	<i>Corr</i>	<i>Pct</i>	<i>RE/Med RE</i>	<i>CE/Med CE</i>	<i>tstat</i>	<i>Pct</i>
Original	0.727	0.000	0.732	0.000	0.748	0.000	0.524/0.522	0.24/0.517	6.960	0.000
1st Diff	0.627	0.000	0.646	0.000	0.642	0.000	0.392/0.389	0.392/0.384	5.889	0.000
Early Calibration										
	<i>Corr</i>	<i>Pct</i>	<i>Corr</i>	<i>Pct</i>	<i>Corr</i>	<i>Pct</i>	<i>RE/Med RE</i>	<i>CE/Med CE</i>	<i>tstat</i>	<i>Pct</i>
Original	0.579	0.000	0.573	0.000	0.544	0.000	0.316/0.309	0.316/0.298	3.305	0.001
1st Diff	0.571	0.000	0.580	0.000	0.605	0.000	0.325/0.319	0.325/0.306	3.992	0.000
Late Verification										
	<i>Corr</i>	<i>Pct</i>	<i>Corr</i>	<i>Pct</i>	<i>Corr</i>	<i>Pct</i>	<i>RE/Med RE</i>	<i>CE/Med CE</i>	<i>tstat</i>	<i>Pct</i>
Original	0.753	0.000	0.757	0.000	0.770	0.000	0.657/0.661	0.187/0.176	3.441	0.001
1st Diff	0.708	0.000	0.716	0.000	0.705	0.000	0.489/0.491	0.487/0.481	5.009	0.000
Late Calibration										
	<i>Corr</i>	<i>Pct</i>	<i>Corr</i>	<i>Pct</i>	<i>Corr</i>	<i>Pct</i>	<i>RE/Med RE</i>	<i>CE/Med CE</i>	<i>tstat</i>	<i>Pct</i>
Original	0.753	0.000	0.757	0.000	0.770	0.000	0.565/0.571	0.565/0.564	5.269	0.000
1st Diff	0.708	0.000	0.716	0.000	0.705	0.000	0.498/0.499	0.498/0.487	4.887	0.000
Early Verification										
	<i>Corr</i>	<i>Pct</i>	<i>Corr</i>	<i>Pct</i>	<i>Corr</i>	<i>Pct</i>	<i>RE/Med RE</i>	<i>CE/Med CE</i>	<i>tstat</i>	<i>Pct</i>
Original	0.569	0.000	0.563	0.000	0.544	0.000	0.622/0.625	0.019/0.003	3.276	0.001
1st Diff	0.571	0.000	0.580	0.000	0.605	0.000	0.317/0.311	0.316/0.291	3.993	0.000
Durbin-Watson of the Full / Early / Late Calibration: 2.310 / 2.563 / 2.035										

Extended Data Fig. 5 | Calibration-verification statistics. Statistical information of the full (1901–2018) calibration model, as well as using two equally-long early/late (1901–1959 and 1960–2018) split period calibration windows, for which the corresponding verification results are provided as well. Each column represents a different measure of interaction between the climate target and proxy variable along with, where appropriate, the probability (Pct) of obtaining that value by chance alone, the exceptions being RE (Reduction of Error), and CE (Coefficient of Efficiency). The four measures are, the Pearson, Robust Pearson, and Spearman correlations, and the statistical significance of the Cross Product (Xprod) between X and Y (Corr = correlation, Med = Median, tstat = *t*-statistic).

20 Wettest Summers

Year (CE)	scPDSI (JJA)	Error (negativ)	Error (positiv)
183	7.80	5.89	9.71
899	7.33	5.65	9.00
728	6.94	4.88	9.01
805	6.89	4.15	9.62
678	6.66	4.73	8.58
725	6.52	4.69	8.38
724	6.53	4.42	8.63
723	6.38	4.24	8.51
171	6.34	3.93	8.74
704	6.33	4.57	8.09
747	6.32	4.52	8.11
212	6.29	4.31	8.28
1107	6.28	4.53	8.02
199	6.27	4.25	8.30
696	6.21	4.48	7.94
806	6.18	3.50	8.87
727	6.08	3.93	8.22
194	6.04	4.33	7.74
370	6.03	4.23	7.82
709	6.02	4.41	7.63

20 Driest Summers

Year (CE)	scPDSI (JJA)	Error (negativ)	Error (positiv)
1992	-3.55	-5.16	-1.94
980	-3.60	-5.26	-1.94
1472	-3.67	-5.32	-2.02
1836	-3.77	-5.54	-2.00
1507	-3.80	-5.49	-2.11
1510	-3.85	-5.60	-2.10
1835	-3.87	-5.57	-2.11
1521	-3.94	-5.65	-2.23
1976	-3.98	-5.72	-2.25
1361	-4.14	-5.81	-2.46
1512	-4.14	-5.93	-2.36
1305	-4.16	-5.78	-2.54
1530	-4.22	-6.07	-2.38
2015	-4.28	-5.93	-2.63
1492	-4.43	-6.18	-2.69
2017	-4.52	-6.12	-2.91
2016	-4.53	-6.22	-2.85
2018	-4.67	-6.36	-2.99
1508	-4.76	-6.45	-3.06
1509	-4.81	-6.58	-3.03

Two Wettest 4yr periods

728	6.12	4.09	8.15
186	5.97	4.07	7.88

Two Wettest 5yr periods

728	6.20	4.12	8.25
187	5.86	3.97	7.75

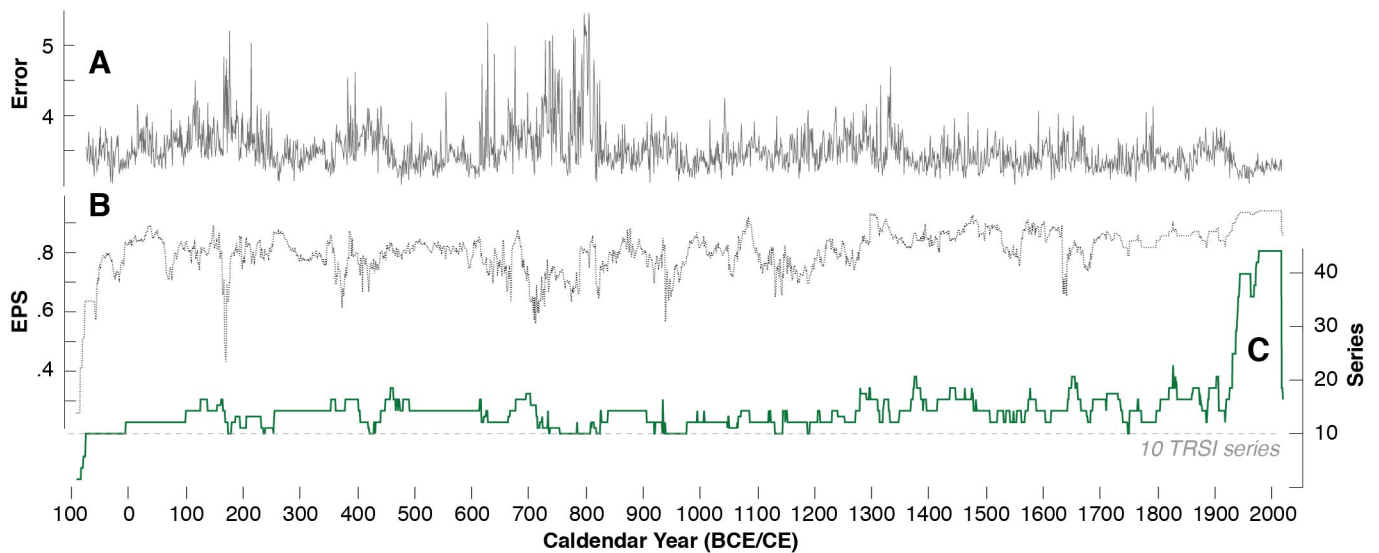
Two Driest 4yr periods

1510	-4.30	-6.03	-2.58
2018	-4.50	-6.16	-2.84

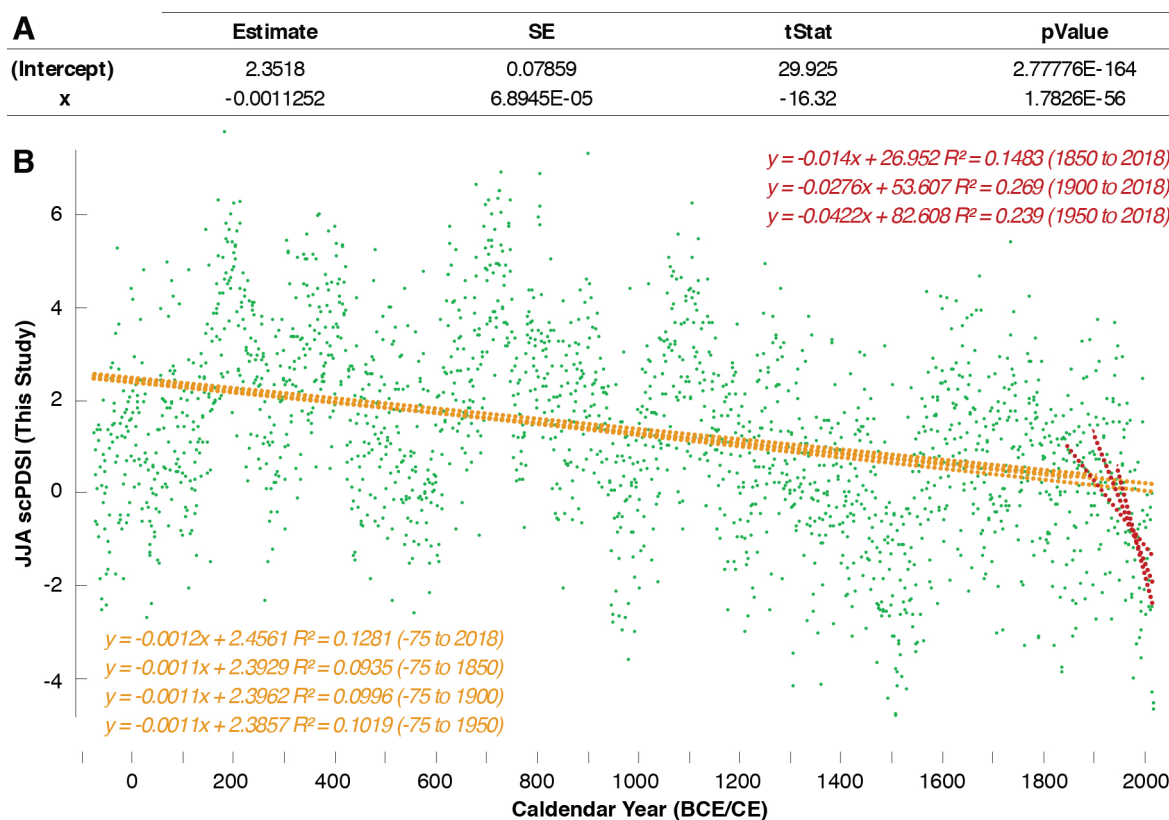
Two Driest 5yr periods

1510	-4.06	-5.77	-2.35
2018	-4.09	-5.74	-2.44

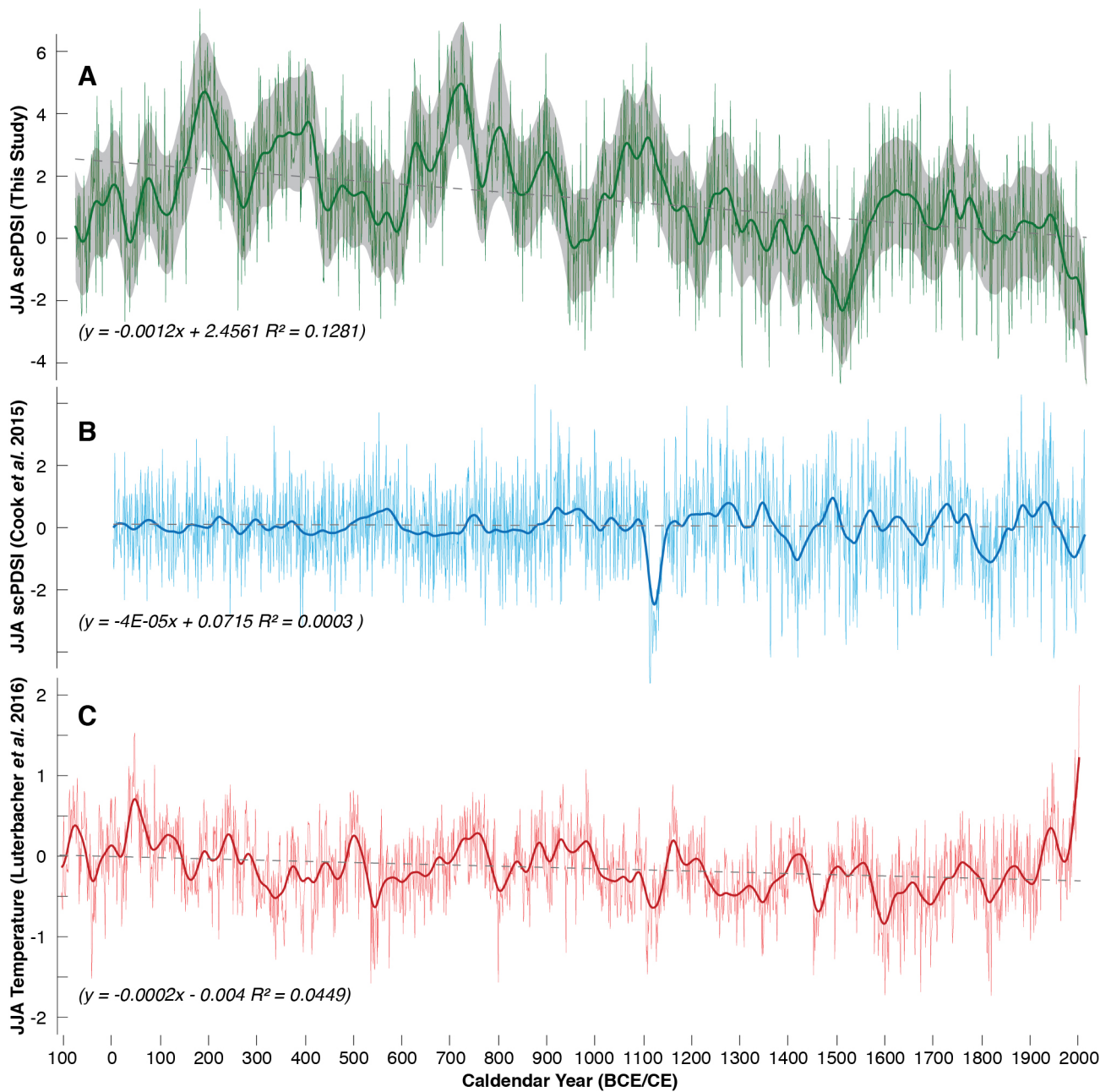
Extended Data Fig. 6 | Reconstructed hydroclimatic extremes. The 20 highest (that is, wettest) and lowest (that is, driest) annual JJA scPDSI values between 75 BCE and 2018 CE (including year zero). The two wettest and driest 4-year and 5-year periods of consecutive JJA scPDSI values (for example, 2018 refers to 2015–2018 and 2014–2018 for the four- and five-year periods, respectively).



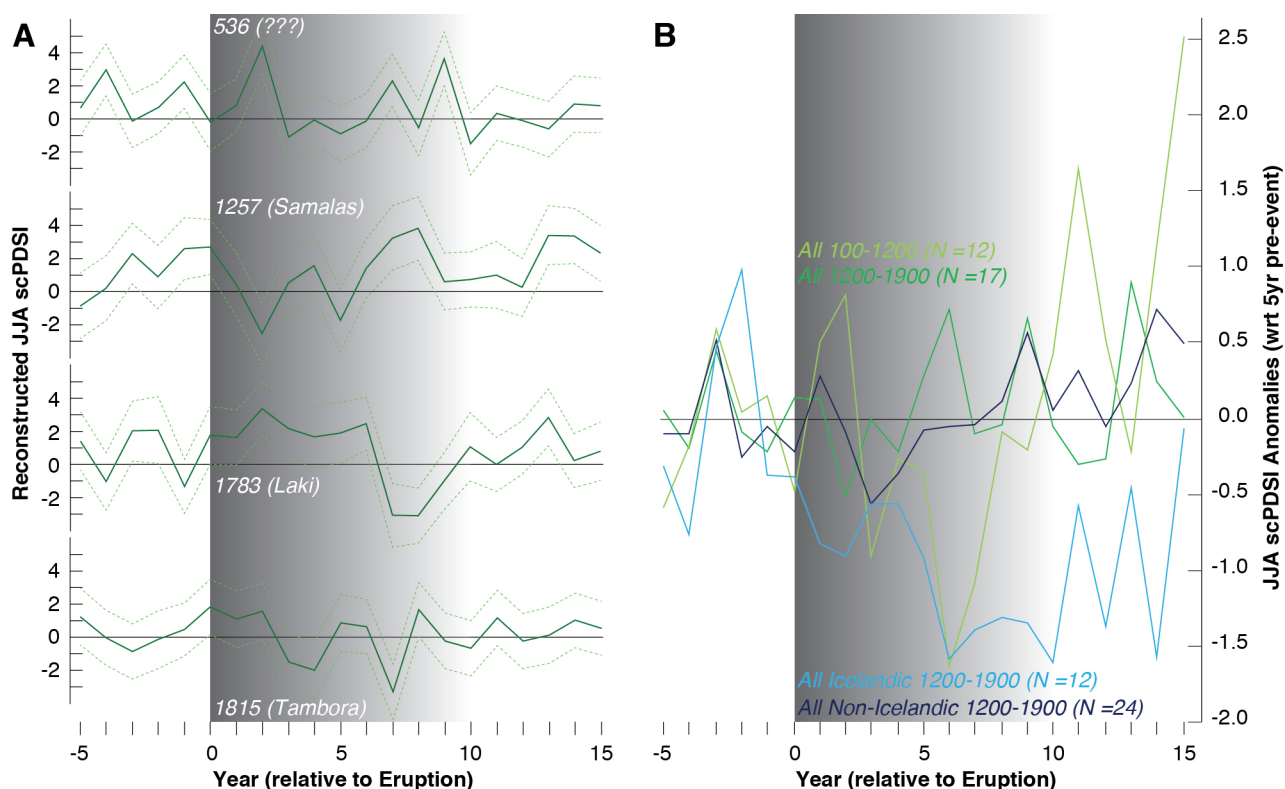
Extended Data Fig. 7 | Reconstruction uncertainty. (a) Temporal evolution of the reconstruction's annual error range that combines measurement (Standard Error) and calibration (Root Mean Squared Error) uncertainties. Note that the error range is consistently decreasing towards present, that is, uncertainty was generally larger in the first half of the Common Era ($y = -0.0001x + 3.6204$, $R^2 = 0.0551$). (b) Expressed Population Signal (EPS) of the combined $\delta^{18}\text{O}$ and $\delta^{13}\text{C}$ dataset (compound TRSI), and calculated over 50-year windows, lagged by 25 years. (c) Sample size of all TRSI ranges between 10 and 42 series per year.



Extended Data Fig. 8 | Trend behaviour. (a) Linear regression fitted to the JJA scPDSI reconstruction from 75 BCE to 2018 CE (with 2094 degrees of freedom). The Root Mean Squared Error (RMSE) is 1.93, the R-squared value is 0.112, the adjusted R-Squared is 0.112, and the F-statistic versus constant model is 266 (p -value = $1.78e-56$). (b) Liner trends of the full the JJA scPDSI reconstruction and three pre-industrial periods (orange), as well as three industrial periods (red). Results from the Mann-Kendall test⁷⁴, modified to account for autocorrelation on the timeseries, reveal there is a significant ($p < 0.01$) negative trend in the reconstructed values.



Extended Data Fig. 9 | Common Era climate history. (a) This study compared against (b) central European JJA scPDSI from the OWDA (ref. ¹²) centred over 49.5°N and 16.5°E, and (c) European JJA temperature anomalies⁴⁶. Thick curves are 50-year cubic smoothing splines and dashed lines long-term trends.



Extended Data Fig. 10 | Volcanic forcing. (a) Reconstructed JJA scPDSI during five periods of strong volcanism. (b) Superposed composites of the JJA scPDSI reconstruction aligned over the 12 (17) strongest individual volcanic forcing events before (after) 1200 CE, as well as using 12 known Icelandic eruptions between 1200 and 1900 CE and a subset of 24 of the strongest non-Icelandic eruptions⁵⁴. Peak volcanic forcing either appears in year zero or year one following the volcanic eruption depending on the latitude and season. Forcing and response are calculated relative to a pre-event 5-year background period presumably undisturbed by volcanic forcing (for example, 1804–1808 for the 1809 and 1815 volcanic eruptions, respectively). Data after secondary eruptions (for example, data from lag +6 years following the 1809 eruption) are removed prior to data aggregation.